

## Numerical study of wind profiles over simplified water waves

Shuyang Cao<sup>1</sup>, Enzhen Zhang<sup>2</sup>, Liming Sun<sup>3</sup> and Jinxin Cao<sup>\*1</sup>

<sup>1</sup>State Key Lab for Disaster Reduction in Civil Engineering, Tongji University, Siping Road 1239, Shanghai, China

<sup>2</sup>School of Civil Engineering, Tongji University, Siping Road 1239, Shanghai, China

<sup>3</sup>Tongji Architectural Design (Group) Co. Ltd, Siping Road 1230, Shanghai, China

(Received February 11, 2015, Revised June 18, 2015, Accepted July 24, 2015)

**Abstract.** Vertical profiles of mean and fluctuating wind velocities over water waves were studied, by performing Large-Eddy Simulations (LES) on a fully developed turbulent boundary layer over simplified water waves. The water waves were simplified to two-dimensional, periodic and non-evolving. Different wave steepness defined by  $a/\lambda$  ( $a$ : wave amplitude;  $\lambda$ : wavelength) and wave age defined by  $c/U_b$  ( $c$ : phase velocity of the wave;  $U_b$ : bulk velocity of the air) were considered, in order to elaborate the characteristics of mean and fluctuating wind profiles. Results shows that, compared to a static wave, a moving wave plays a lesser aerodynamic role as roughness as it moves downstream slower or a little faster than air, and plays more aerodynamic roles when it moves downstream much faster than air or moves in the opposite direction to air. The changes of gradient height, power law index, roughness length and friction velocity with wave age and wave amplitude are presented, which shed light on the wind characteristics over real sea surfaces for wind engineering applications.

**Keywords:** large-eddy simulation; wave age; wave amplitude; wind profiles

### 1. Introduction

Wind load codes/specifications usually consider sea exposure as the smoothest condition of ground roughness, and specify the smallest power law index for mean velocity profile near the coast (for example, AIJ-RLB-2004, ASCE7-10). However, sea waves play aerodynamic roles as surface roughness when a turbulent boundary layer is developing over the sea surface. Unlike roughness on land, a wave's aerodynamic performance is not fixed because it moves and its shape changes continuously even during a single wind event, which makes the wind profile over a sea wave very complicated. Many field measurements have shown that sea surface wind stress, drag coefficient and aerodynamic roughness length are dependent on the coupling effect of wind-wave interaction (e.g., Charnock 1955). Powell *et al.* (2003) analyzed wind velocity profiles over oceans measured by GPS sonde during tropical cyclones and reported reduced drag coefficients for high wind speeds. This means that the roughness length does not increase with increase in wind speed at high wind speeds. Zachry *et al.* (2013a) studied the drag coefficient over a fixed shoaling

---

\*Corresponding author, Assistant Professor, E-mail: [jinxin@tongji.edu.cn](mailto:jinxin@tongji.edu.cn)

hurricane wave train by laboratory measurements while Zachry *et al.* (2013b) conducted a case study of near shore drag coefficient behavior during a hurricane. Similar to Powell *et al.* (2003), Zachry *et al.* (2013a, 2013b) paid attention to the dependence of drag coefficient on wind speed and wave condition. The sophisticated air flow field over waves is in great need of investigation as a guarantee of human offshore activities and facilities involved with oceans, such as oil and natural gas exploitation, long-span sea bridges and offshore wind turbine farms that are sensitive to wind loads. Thus, mean and fluctuating velocity profiles as well as the turbulent structure of atmospheric boundary layers over waves are important and urgent issues for wind engineers.

The air-sea interface is a complex system of interacting waves and atmospheric turbulence over a wide variety of spatial and temporal scales. The exchange of momentum and energy across the sea surface, for the most part, occurs on a molecular scale, involving both turbulent and laminar processes modified by wave breaking, surface tension, the structure of the wind boundary layer, and the ocean mixed layer, among other effects. No complete theory of wind-wave generation and growth has been formulated till now. Although oceanographers and meteorologists have conducted many studies focusing on sea surface wind stress, drag coefficient and aerodynamic roughness length (Charnock 1955, Toba *et al.* 1990, Smith *et al.* 1992, Johnson *et al.* 1998, Drennan *et al.* 2004, Zachry *et al.* 2013b), parameterization of wind stress and wind profile still remain controversial (Jones and Toba, 2001). In order to better parameterize sea-air interaction, besides a large volume of field measurements, there have been several laboratory and numerical studies that have idealized or simplified the flow configuration by assuming the sea surface to be two-dimensional and non-evolving, and studied the influence of imposed sinusoidal wave motion on the upper flow field while neglecting the effects of other factors such as wave breaking, wave evolvment and surface tension. For instance, Sullivan *et al.* (2000, 2002, 2008) simplified the sea wave and studied the influences of thermal stratification and non-equilibrium state on turbulent flow over sea waves based on Couette-flow approximation from the meteorological viewpoint. Interaction between wave surface and atmosphere, particularly surface tension and momentum transfer from the ocean to the atmosphere, have been studied, but the vertical profiles of mean and fluctuating wind profiles, which are important for wind-resistant design of structures and wind energy utilization, were not involved. Recently, Chen and Letchford (2007) investigated experimentally the flow over a moving wavy surface by installing a moving belt on the floor of a wind tunnel. They found that there is a trend of decreasing roughness with wave age. However, the moving belt system simulates a translational motion of wavy surface, so whether their results are applicable to a wave motion is questionable. Recently, Zachry *et al.* (2013a) made laboratory measurements of the drag coefficient over a fixed shoaling hurricane wave train, and reported a higher value than that in hurricane conditions. Insufficient understanding of wind characteristics over sea waves motivated the present study.

In the present study, the turbulent boundary layer over water waves was studied numerically. Water waves were simplified as two-dimensional, periodic, and non-evolving, as Sullivan *et al.* (2000) and Chen and Letchford (2007). The wave surface elevation  $h$  is a function of both the  $x$  coordinate value and time  $t$ , and is expressed as  $h(x,t) = a \sin k(x-ct)$ , where  $a$  is wave amplitude,  $k$  is wave number ( $k = 2\pi / \lambda$ , where  $\lambda$  is wavelength), and  $c$  is phase speed of the wave. The present study assumed that the sea wave was non-evolving, so all wave parameters including wave amplitude, wavelength and phase velocity did not change with time. In addition to wave amplitude, another important parameter discussed in the present study is wave age, which is defined as  $\beta = c / U_b$ , where  $U_b$  is a representative velocity of the air defined later. Wave age describes the

evolution state of a sea wave. Take the sea wave at a location experiencing a typhoon as an example to explain the meaning of wave age. A sea wave emerges and grows under the stimulation of strong wind with  $0 < \beta < 1$  (wave follows wind), and gradually gains phase speed until it finally turns into a mature sea with large phase speed. When the typhoon eye approaches, the wave may move faster than the wind due to the reduction of wind speed, i.e.,  $\beta > 1$  (wind follows wave). It is also possible for the wind direction to reverse after passage of the typhoon eye and yield negative wave age  $\beta < 0$  (wave opposes wind). In this study, the dependence of the atmospheric boundary layer over waves on both wave age and wave steepness was investigated systematically, by considering three wind amplitudes (low, medium and high) and eight wave ages belonging to three wave age categories (wave moves upstream against wind, and downstream with a speed slower or faster than wind). Particular attention was devoted to the variation of gradient height, power law index, roughness length and friction velocity of the boundary layer with wave age and wave amplitude. This study aimed to shed light on the wind characteristics off the coast for wind engineering applications.

In the present study, an unsteady three-dimensional large-eddy simulation of incompressible turbulent flow over waves was performed by using an open source software package OpenFOAM (2012). The options and solvers offered by OpenFOAM were carefully selected in order to achieve reliable simulation results. A user-defined solver was developed for the present study by integrating two standard solvers of OpenFOAM, which were channelFoam and pimpleDyMFoam that were able to deal with the channel flow and dynamic mesh, respectively. Several supplementary calculations on flow over static and moving wavy surfaces, where experimental or numerical results were available for comparisons, were carried out to validate the user-defined solver.

In this paper, the governing equations, numerical method as well as computational domain and grid system, boundary and initial conditions, and the statistical method are described first, followed by detailed validations. Then, the phase-averaged flow features of the turbulent boundary layer over moving wavy surfaces are illustrated. Finally, the profiles of mean and fluctuating wind speed over waves are provided, together with estimations of gradient height, power law index and roughness length, as well as their variations with wave age and wave amplitude.

## 2. Problem formulation and numerical method

### 2.1 Flow configuration

The flow considered is a three-dimensional turbulent boundary layer flow over a simplified two-dimensional solid wave with a phase speed  $c$  that can be either downstream or upstream. A sketch showing the flow orientation, coordinate system, wavy lower boundary and boundary conditions is given in Fig. 1. A coordinate system, where  $x$  is aligned with the primary flow direction,  $y$  is measured vertically from the mean wave elevation and  $z$  is the spanwise direction parallel to wave crests and troughs, is adopted. The Reynolds number defined as  $Re = U_b \times \lambda / \nu$  is 10000, where  $\nu$  is the kinematic viscosity and  $U_b$  is the bulk velocity defined as

$U_b = \frac{1}{H-h} \int_h^H u dy$ . The bulk velocity  $U_b$  is maintained at  $U_b = 1$  by adapting a pressure gradient in the  $x$  direction dynamically with an addition to or subtraction from pressure gradient as

$U_b$  falls below or exceeds 1.0, so there are no Reynolds number effects for any investigated combinations of wave amplitude and wave age.

In this study, three wave-amplitude-to-wavelength ratios,  $\xi = a/\lambda = 0.025, 0.05$  and  $0.075$ , representing low, medium and high wave amplitudes, were considered. According to linear wave theory, a wave steepness higher than  $1/14$  would result in the wave crests overtaking the wave, i.e., the wave would break (Niclasen *et al.* 2010). Therefore, the maximum wave steepness of the present study was selected to be  $0.075$ . For each amplitude-to-wavelength ratio, eight wave-age values were adopted,  $\beta = c/U_b = -1.5, -1.0, -0.5, 0.5, 0.75, 1.0, 1.5$  and  $2.0$ , in which  $\beta = -1.5, -1.0$  and  $-0.5$  represented the situation of wave opposing wind,  $\beta = 0.5, 0.75$  and  $1.0$  represented the situation of wave following wind, and  $\beta = 1.5$  and  $2.0$  represented the situation of wind following wave. A static wave was also simulated in order to provide data for comparison to show the effects of wave motion. It is noteworthy that the value of wave age of a mature wave developing over an open sea usually falls in a certain region, if the wave has reached to an equilibrium condition. For instance, a bulk measure of wind-wave equilibrium is when the ratio of the peak phase speed of the wave-height spectrum to a reference atmospheric wind attains a limiting value of  $1.2$  (Alves *et al.* 2003). It implies that the majority of the assumed wave ages of the present study correspond to non-equilibrium conditions. However, these non-equilibrium conditions such as negative wave age do exist in a real sea. In the present study, simulations were performed with respect to various combinations of wave number and wave amplitude in order to elaborate the characteristics of the mean and fluctuating wind speed profiles over waves.

## 2.2 Governing equations and numerical method

The governing equations of large-eddy simulation are the filtered three-dimensional continuity equation and Navier-Stokes equations on momentum conservation. The momentum conservation equation of filtered variables can be written as

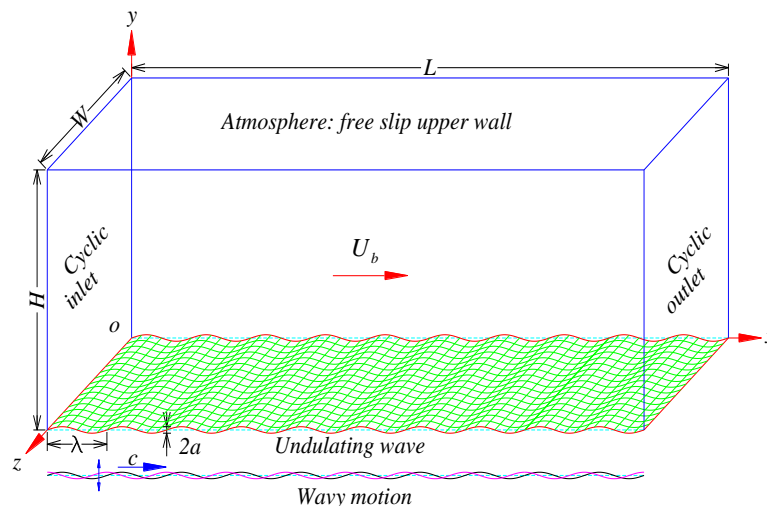


Fig. 1 Sketch of three-dimensional flow

$$\frac{\partial \mathbf{U}}{\partial t} + \nabla \cdot (\mathbf{U}\mathbf{U}) = -\frac{1}{\rho} \nabla p + \nabla \cdot \mathbf{v}(\nabla \mathbf{U} + \nabla \mathbf{U}^T) + \nabla \boldsymbol{\tau} + \mathbf{P} \quad (1)$$

together with the mass conservation equation

$$\nabla \cdot \mathbf{U} = 0 \quad (2)$$

where the filtered velocity vectors  $\mathbf{U} = (u, v, w)^T$  are the three velocity components in a Cartesian physical space.  $\nabla \cdot ()$  and  $\nabla ()$  are divergence operator and gradient operator, respectively.  $\mathbf{P} = (P_x, 0, 0)^T$  is a dynamically adjusted uniform pressure gradient vector that drives the flow in the  $x$  direction and  $\boldsymbol{\tau}$  is the sub-grid stress tensor. The grid scale turbulence is solved while the sub-grid scale turbulence is modeled. A dynamic Smagorinsky-Lilly model is used for the sub-test scale stress tensor (Lilly 1992), which is given by

$$\begin{cases} \boldsymbol{\tau} = \frac{2}{3} k \mathbf{I} - 2\nu_{SGS} \text{dev}(\mathbf{S}) \\ k = C_I \Delta^2 \|\mathbf{S}\|^2 \\ \nu_{SGS} = C_D \Delta^2 \|\mathbf{S}\|^2 \end{cases} \quad (3)$$

where  $\mathbf{S} = 1/2(\nabla \mathbf{U} + \nabla \mathbf{U}^T)$  is the rate of strain tensor of the filtered field,  $k$  is the sub-grid scale kinetic energy, and  $\Delta$  is the grid filter scale deviatoric component of  $\mathbf{S}$  is given by

$$\begin{cases} \text{dev}(\mathbf{S}) = \mathbf{S} - \frac{1}{3} \text{tr}(\mathbf{S}) \\ \text{tr}(\mathbf{S}) = S_{11} + S_{22} + S_{33} \end{cases} \quad (4)$$

and other parameters are given by

$$\begin{cases} C_I = \frac{\langle Km \rangle}{\langle mm \rangle}, K = 1/2(\overline{UU} - \overline{U}\overline{U}), m = \Delta^2(4\|\overline{\mathbf{S}}\|^2 - \|\mathbf{S}\|^2) \\ C_D = \frac{\langle L \cdot M \rangle}{\langle MM \rangle}, L = \text{dev}(\overline{UU} - \overline{U}\overline{U}), M = \Delta^2(\|\overline{\mathbf{S}}\|^2 - 4\|\mathbf{S}\|^2) \end{cases} \quad (5)$$

where the over-bar denotes “test” filtered.

Central differencing was applied for both convection and diffusion terms, and non-orthogonal correction was used for gradient. Second order backward differencing was chosen for temporal derivative discretization. The PISO algorithm (Issa 1986) was adopted to deal with pressure-velocity coupling. An adjustable time step was used to ensure a maximum Courant number of 0.5, while in the calculation cases of  $\beta > 1$ , a more strict CFL condition was applied to ensure a Courant number of no more than 0.25, in order to avoid computation explosion. A dynamic-mesh solver was compiled by adding a sub-solver to solve mesh motion simultaneously and update the grid points for each time step. Convergence of iteration was deemed to be achieved,

with tolerance of  $10^{-7}$ ,  $10^{-6}$  and  $10^{-8}$  for pressure, velocity and cell displacement, respectively.

### 2.3 Computational domain and grid system

As illustrated in Fig. 1, the computational domain size is  $(L, H, W)=(10\lambda, 4\lambda, 2\lambda)$  with  $\lambda=1$ , in the  $x$ ,  $y$  and  $z$  directions, respectively, which has been proved sufficiently larger than the largest eddy in question by checking the two-point correlation coefficient in all three directions (Shen *et al.*, 2003). The computational domain is spatially resolved by a structured grid system with  $(N_x, N_y, N_z)=(320, 88, 48)$ , in which the grid lines in the  $x$  direction are surface-fitted and those in the other two directions are along the  $y$  and  $z$  directions, respectively. Thus, the grids in the  $x$ - $z$  and  $y$ - $z$  planes are orthogonal. Evenly distributed grids are applied in the  $x$  and  $z$  directions, while a dense clustering of grid points is applied near the underlying wavy surface in the  $y$  direction, with  $y^+$  of the first grid fitted to the surface being less than 1.0 during the calculation. The grid size in the  $y$  direction stretches outwards and grid lines change gradually away from the wave surface into straight lines on the top. Only the grid size in the  $y$  direction is re-allocated when the waves are moving. The Reynolds number is 10000.

### 2.4 Boundary condition and initial condition

As shown in Fig. 1, a free-slip condition is applied for both the velocity and pressure on the upper boundary. A periodic boundary condition is imposed for both the velocity and pressures on the streamwise and lateral boundaries, so a fully-developed turbulent boundary layer can be achieved after recycling the flow in the streamwise direction sufficiently. A no-slip condition on the bottom is achieved by letting the flow velocity on the wavy boundary equal the velocity of the moving surface. The velocity of the moving wave surface is obtained from a time derivative of wave surface elevation, which is expressed as  $U_{wall}=(0, -\omega a \cos k(x-ct), 0)$  in the  $x$ ,  $y$  and  $z$  directions, where  $\omega = kc$  is the frequency of wave motion. The boundary condition at the bottom describes a travelling wave upon which every particle oscillates up and down about its equilibrium position.

As the initial condition, a transition entry  $F(t)=1-\exp(-t^2)$  that fulfils a gradual transition from 0 to 1 in a relatively short time (Shen *et al.*, 2003) is added to the wave shape, in order to avoid a sudden jump of the flow configuration from a flat open channel to a wavy one. Thus, the wave surface elevation during the calculation is actually  $h(x,t)=a \sin k(x-ct)[1-\exp(-t^2)]$ .

Statistical processing was performed after  $t=80\lambda/U_b$  which is long enough to give fully developed flow fields, and another  $220\lambda/U_b$  (22 flow-through time) is consumed to obtain converged statistical results. Averaging was done spatially first along the spanwise direction, then over the same phase angle of ten wavelengths in the  $x$ -direction when the phase-averaged flow structure was calculated. However, when the wind profiles are calculated, averaging was performed over the horizontal plane according to customs in the field of wind engineering, so only the velocity information at heights higher than the wave amplitude are available.

## 3. Validation

A user-defined solver that integrates several standard solvers offered by OpenFOAM is developed for the purpose of the present study. Therefore, both the standard solvers and user-defined solver had to be validated in order to achieve reliable simulation results. Because there were no experimental or field data available on turbulent flow over simplified waves, the validations were performed by comparing first turbulent flows over a static wave and then moving waves with a dynamic mesh with numerical results of available references, which are described as follows.

### 3.1 Flow over static wavy surface

Numerical fundamentals including a discretization scheme, a pressure-velocity coupling algorithm, a turbulence model and a boundary condition setting were expected to be validated by simulating turbulent flow over a static wave. A solver channelFoam provided by OpenFOAM was used to simulate the flow around a static wavy surface that was driven by a pressure gradient. The simulation was performed by adopting a dynamic Smagorinsky-Lilly model, and periodic boundary conditions in the streamwise and spanwise directions. There were plenty of data available that could be used to validate the present simulation because many laboratory experiments and numerical simulations had been performed on turbulent flow over a static sinusoidal wall. As examples, Fig. 2 compares the distributions of phase-averaged friction drag and pressure drag of a wavy channel flow obtained by the present simulation by utilizing channelFoam with the experimental data (Buckles *et al.* 1984). Friction drag  $\tau_w$  and pressure drag  $p_w$  are representative parameters illustrating the interaction between waves and air, which are defined as  $\tau_w = \tau_0 / (0.5\rho U_b^2)$ , where  $\tau_0 = \mu \times (dU / dy)|_{wall}$  is the friction force on the wall, and  $p_w = (p_0 - p_{ref}) / (0.5\rho U_b^2)$ , where  $p_0$  and  $p_{ref}$  are the pressures on the wall and upstream pressure, respectively. The ratio of amplitude to wavelength of the example is 0.05. The Reynolds number of the simulation is the same as that of the experiment (Re=6760). The results obtained by simulation and experiment exhibit similar flow features as follows. Fig. 2(a) shows that friction force  $\tau_w$  is negative between  $x/\lambda \approx 0.14$ -0.66, corresponding to a recirculation zone formed on the down slope of the static wave due to a large-scale flow separation. The friction force becomes positive on the upslope of the wave and increases rapidly due to increase in velocity gradient, causing a maximum value at  $x/\lambda \approx 0.917$ . Fig. 2(b) shows that the pressure is positive between  $x/\lambda \approx 0.42$ -0.87, with a maximum positive pressure at  $x/\lambda \approx 0.71$ . The pressure at other locations is negative due to flow recirculation, with a maximum negative pressure appearing near the crest. In addition, the pressure drag force is one order greater than that of the friction drag force. Fig. 2 shows that the results of the present simulation agree reasonably well with the experimental data, indicating that the numerical method of the present simulation is generally acceptable.

### 3.2 Flow over moving wavy surface

The standard channelFoam provided by OpenFOAM does not support the calculation based on a dynamic mesh. Thus, we developed a new solver that integrates the functions of channelFoam and pimpleDyMFoam, which is another solver provided by OpenFOAM that can deal with a dynamic mesh, for the purpose of the present calculation. This user-defined solver was validated

by comparing the flow field over moving waves with those obtained by Shen *et al.* (2003) at the same flow parameters as  $\beta = 0.4$ ,  $\xi = 0.04$  and  $Re = 10000$ , although Shen *et al.* (2003)'s work was conducted without turbulence models. Fig. 3 compares the streamline, and contours of longitudinal and vertical mean velocities of the flow field with those of Shen *et al.* (2003). Fig. 3(a) shows that, in both the present study and Shen *et al.* (2003), streamlines are emitted from the downslope and absorbed into the upslope. The discrepancy of the position of contour lines of longitudinal velocity for 0.5 and larger values can be noticed in Fig. 3(b), while the discrepancy in the vertical velocity can also be noticed away from the wave surface in Fig. 3(c).

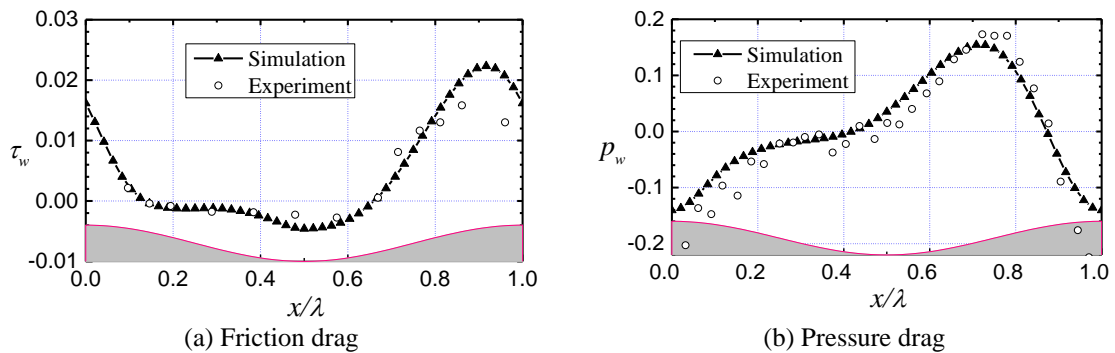


Fig. 2 Comparison of friction and pressure distributions over wavy surface with the experiment data (Buckles *et al.* 1984)

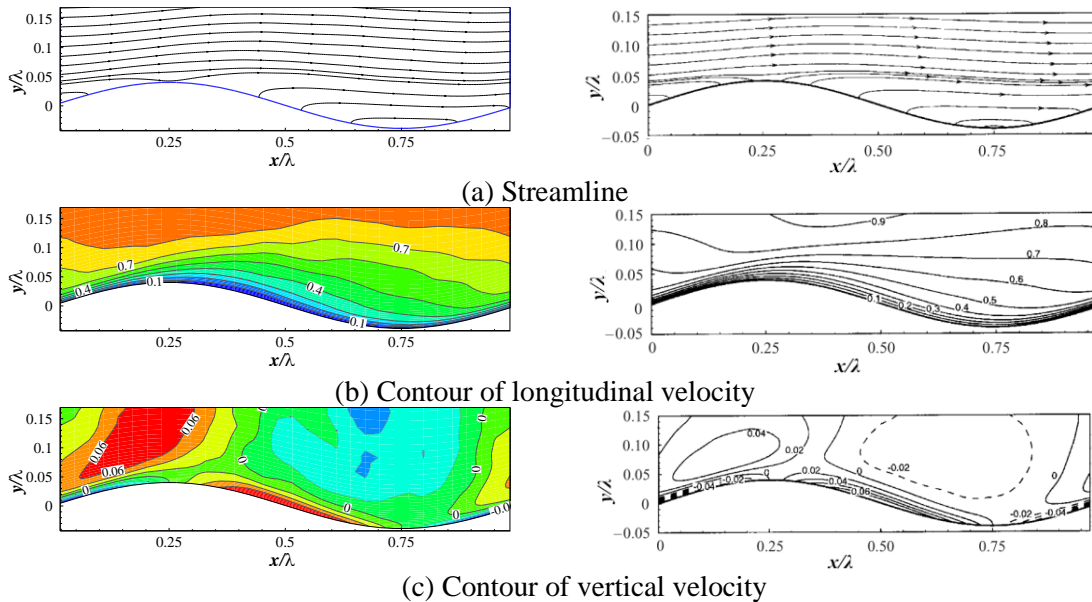


Fig. 3 Comparisons of flow fields (Left: the present study; Right: Shen *et al.* (2003))

However, the flow structures near the wave surface present good consistency, implying that the user-defined solver can deal with the problem of moving waves with a dynamic mesh. Thus, this user-defined solver, together with the simulation parameters including grids, initial conditions, boundary conditions and turbulence models, was applied to the calculations with the moving surface of the present study.

### 3.3 Grid dependence

As described above, the simulations of turbulent flow over waves in the present study were performed with a structured grid system of  $(N_x, N_y, N_z)=(320, 88, 48)$ . In order to examine the grid dependence of the simulation, a flow with a wave age of  $\beta=1.5$  was also simulated with a denser grid system of  $(N_x, N_y, N_z)=(400, 116, 60)$ . The reason for choosing the case of  $\beta=1.5$  as an example to examine the grid dependence was because the turbulent intensity near the wave surface was higher at this wave age, which is shown later. Fig. 4 compares the profiles of time-averaged mean velocity  $\bar{U}$  obtained for the two grid systems. It can be seen that the solutions from the two grid systems show very little difference, implying that the grid number of  $(N_x, N_y, N_z)=(320, 88, 48)$  with specified grid distributions can give satisfactory grid-independent results.

## 4. Results and discussion

### 4.1 Phase-averaged flow fields

Although the present study focuses on wind profiles over simplified waves, variation of phase-averaged flow fields with wave age and wave amplitude are illustrated respectively in Fig. 5 and Fig. 6, in order to help understanding of the results of wind profiles shown later. Fig. 5 illustrates the variation of phase-averaged streamlines with wave age at a wave amplitude of  $\xi=0.05$ , in which  $\beta=-0.5, 0.5$  and  $1.5$  represent the categories of wave opposing wind, wave following wind and wind following wave, respectively. The results obtained for a static wave are shown together for comparison. It can be found that a moving wave results in a flow structure that is significantly different than that of a static wave. A recirculation bubble forms on the down slope in the case of a static wave (Fig. 5(b)) due to flow separation. However, the wave surface is no longer a streamline due to the existence of vertical velocity on the wave surface in moving waves. The streamline patterns change with wave age because the vertical velocity component on the wave surface is proportional to the wave age. In Fig. 5(a), where the wave age is minus, the upslope emits streamlines that separate into two bundles; one moves upstream and the other downstream and they finally converge above the downslope, which sucks in the streamlines with a relatively low pressure. A negative horizontal velocity component covers almost the whole trough while the vertical velocity component is positive upslope and negative downslope and distributes anti-symmetrically about the crest where the vertical component equals zero. However, in cases of positive phase speeds, streamlines are emitted from the downslope and absorbed into the upslope. The influenced height becomes larger and a vertical flow trend becomes more evident with increase in wave age. Inverse flows are noticed above crest where minimum pressure is located when  $\beta=1.5$  and the vertical velocity becomes more symmetric about the wave crest. Fig. 6 presents variations of phase-averaged streamline with wave amplitude at a negative wave number

( $\beta = -0.5$ ) and a positive wave number ( $\beta = 0.5$ ). Qualitatively-similar flow structures are noticed at different wave amplitudes for each wave number, implying that the wave amplitude is not a dominant parameter in determining the flow structure. These flow features influence the velocity profiles over waves.

4.2 Variation of mean velocity profile with wave age and wave amplitude

Figs. 7(a)-7(c) illustrate the variation of mean velocity profile with wave age at different wave amplitudes,  $\xi = 0.025, 0.05$  and  $0.075$ , respectively. Note that both the vertical profile of mean velocity  $\bar{U}$  shown here and the vertical profile of fluctuating velocity  $u'$  shown later are obtained by conducting averaging over horizontal plans in addition to time averaging, and only the velocity information at heights higher than wave amplitude are available.

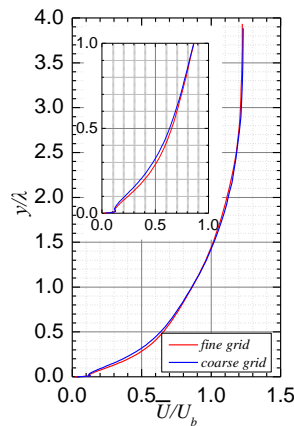


Fig. 4 Comparison of mean velocity profiles computed from two grid systems

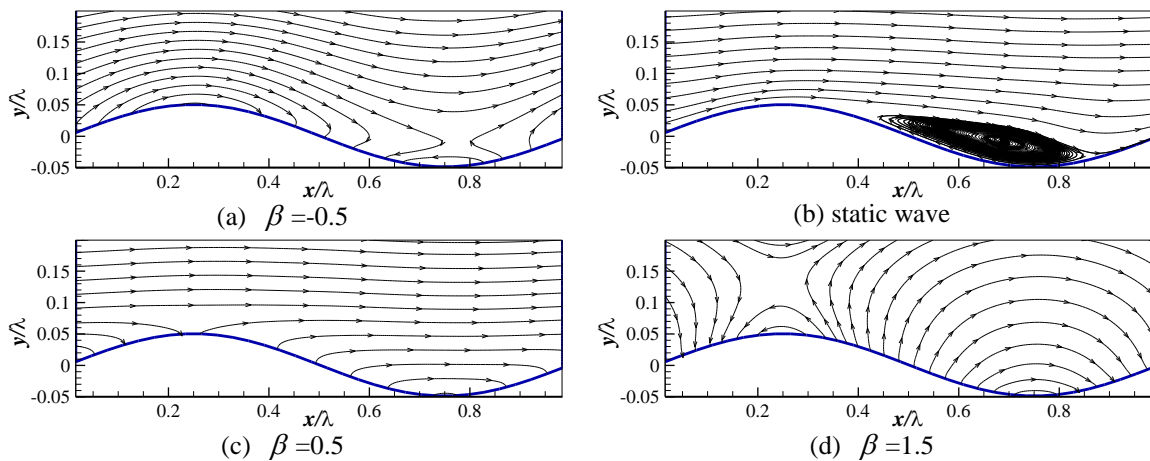


Fig. 5 Variation of phase-averaged streamlines with wave age ( $\xi = 0.05$ )

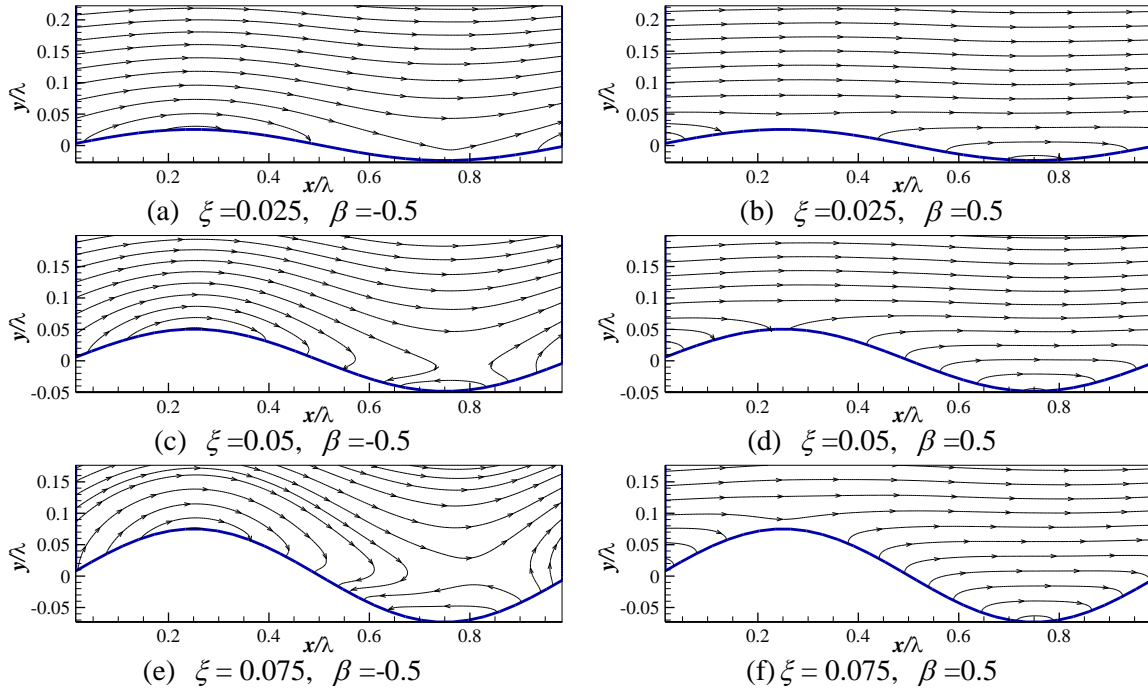


Fig. 6 Variation of phase-averaged streamlines with wave amplitude (Left:  $\beta = -0.5$ ; Right:  $\beta = 0.5$ )

The value on the  $y$  axis represents the elevation from the equilibrium position of the wave. In Figs. 7(a)-7(c) for different wave amplitudes, the vertical profiles are illustrated with respect to three groups of wave age:  $-1.0 \leq \beta < 0$ ,  $0 < \beta < 1.0$  and  $1.0 \leq \beta < 2.0$ . The mean velocity profiles of the turbulent boundary flow over static waves are shown together for comparison.

Figs. 7a, 7b and 7c show that, generally, when  $0 < \beta < 1.0$ , the flow velocity near the wave surface is greater than that of a static wave, and increases with increase in wave age. Meanwhile, the boundary layer height is lower than that over a static wave. These results imply that a moving wave plays a lesser aerodynamic role as roughness than a static wave when  $0 < \beta < 1.0$ . When  $1.0 \leq \beta < 2.0$ , the flow velocity near the wave surface is smaller than that at  $\beta = 1.0$ , and decreases with increase in wave age, implying that the wave plays a more aerodynamic role than that at  $\beta = 1.0$ . Note that the flow velocity near the wave surface at  $\beta = 1.0$  is greater than that of a static wave, and the velocity profile at  $\beta = 1.5$  is very close to that of a static wave. When  $-1.0 \leq \beta < 0$ , the flow velocity near the surface is smaller than that of a static wave, and decreases with increase in the absolute value of wave age, implying that a wave with an age of  $-1.0 \leq \beta < 0$  plays a more aerodynamic role than that of a static wave. With increase in the absolute value of wave age, the gradient height increases, and the deformation of velocity profiles extends to higher elevations of the computational domain.

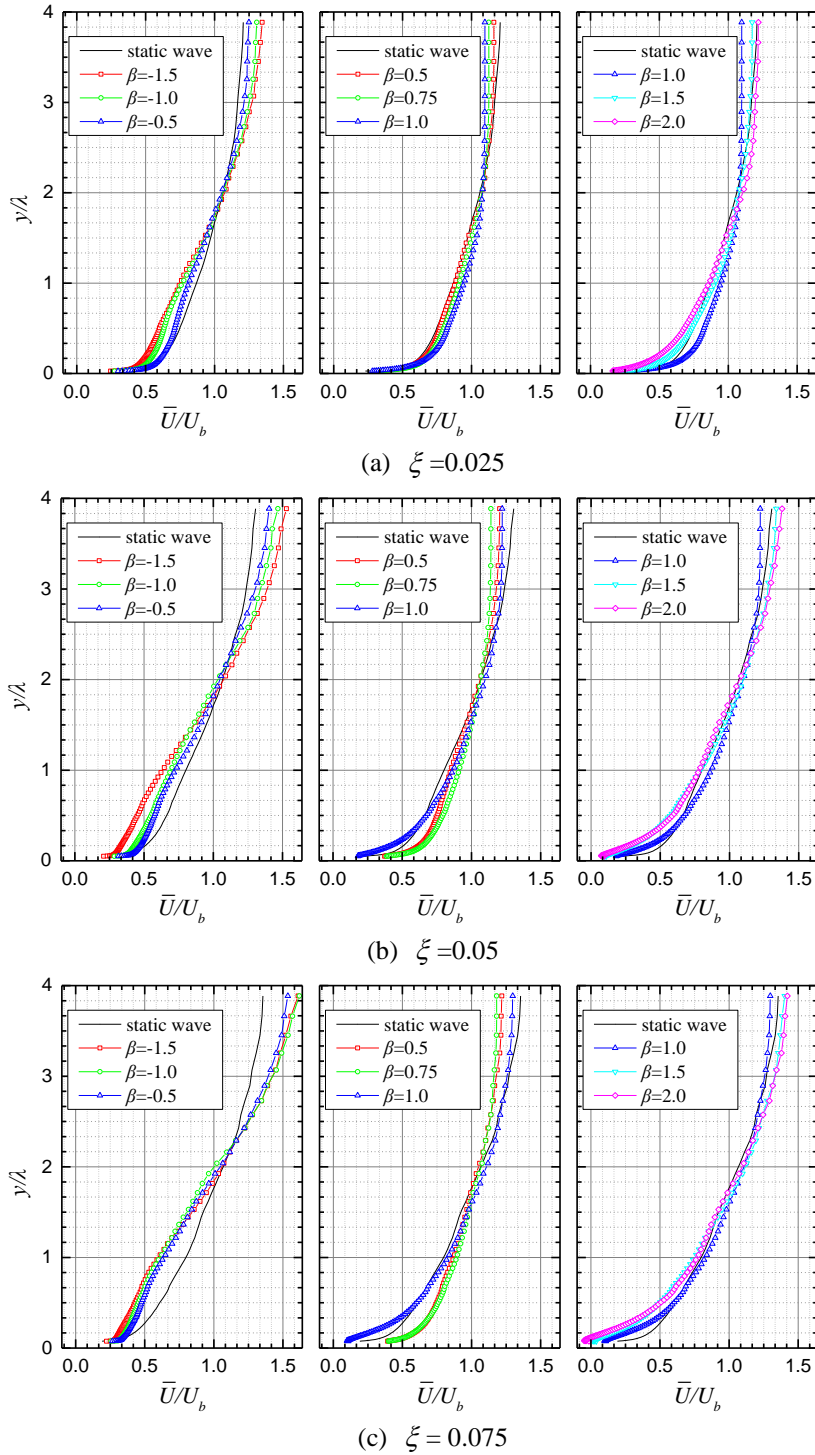


Fig. 7 Variation of mean velocity profiles over waves with wave age at different wave amplitudes

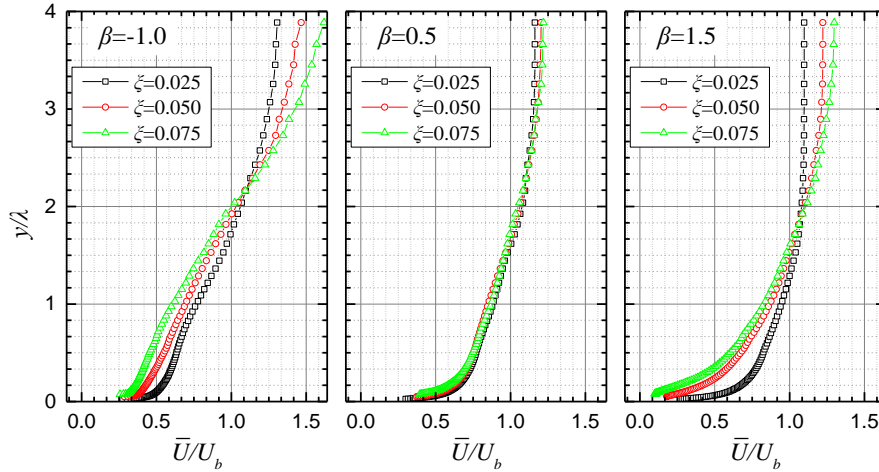


Fig. 8 Variation of mean velocity profile over waves with wave amplitude at different wave ages

The mean velocity profiles at different wave amplitudes obtained at wave ages of  $\beta = -1.0, 0.5$  and  $1.5$  in Fig. 7 are re-plotted in Figs. 8(a)-8(c) to show the variation of mean velocity profile with wave amplitude. A greater value of wave amplitude corresponds to a steeper wave shape, which brings more significant vertical movement of the wave and influences the interaction at the interface more significantly. It is well-known that wave amplitude is a critical parameter in determining the turbulent boundary layer over static waves because large scale separation occurs at the down slope of a static wave if the down slope is steep enough to cause flow separation. However, in the moving wave mode, at the wave surface the longitudinal velocity is zero while the vertical velocity is proportional to wave age, so the wave amplitude is not as important in determining the flow structure as it is for a static wave. Although Fig. 6 shows that the flow structures at different wave amplitudes are analogous to each other at a fixed wave age, the difference of velocity profile due to wave age becomes more significant when the wave amplitude becomes larger, as shown in Fig. 7. In addition, it can also be found in Fig. 8 that, with the increase in wave amplitude, both gradient velocity and gradient height increase. The wave becomes aerodynamically rougher with increase in wave amplitude at  $\beta = -1.0$  and  $1.5$ , while the dependence of mean velocity profile on wave amplitude is not significant at  $\beta = 0.5$ .

Fig. 9 presents velocity profiles that are curve-fitted to power law expressions with the mean velocity being normalized by gradient wind speed  $U_g$ . The velocity profiles of different wave ages obtained at  $\xi = 0.05$  are shown as examples. The power law expression of mean velocity

profile is  $\bar{U}(y) = \left( \frac{y}{H_r} \right) U_r$ , where  $U_r$  is the reference wind speed at reference height  $H_r$ . It is

obvious that the velocity increases fast with increase in height, and the vertical velocity profile generally approaches a power law expression at positive wave ages. However, when the wave age is negative, the velocity increases with height almost linearly, and clearly deviates from the power law at heights lower than  $y/\lambda < 1$ . Attempts were made to fit all velocity profiles to power law

expressions including those for negative wave ages. The reference height was taken at  $H_r / \lambda = 2.0$  because it was considered better to select the same reference height for all investigated wave ages. Note that this curve fitting for the velocity profiles of negative wave ages guarantees conservative wind loads for wind resistant design of structures, as shown in Fig. 9. Meanwhile, Fig. 10 presents the velocity profiles fitted to a log law expression, which is expressed as  $\bar{U} = \frac{u_*}{k} \ln\left(\frac{y-h_d}{z_0}\right)$ , where  $u_*$ ,  $z_0$  and  $h_d$  are the friction velocity, roughness length and zero-displacement, respectively, which are obtained by least-square fitting to the log law expression. As in Fig. 9, the velocity profiles of different wave ages obtained at  $\xi = 0.05$  are shown in Fig. 10 as examples. Fig. 10 shows that the log law expression generally stands for all investigated wave ages.

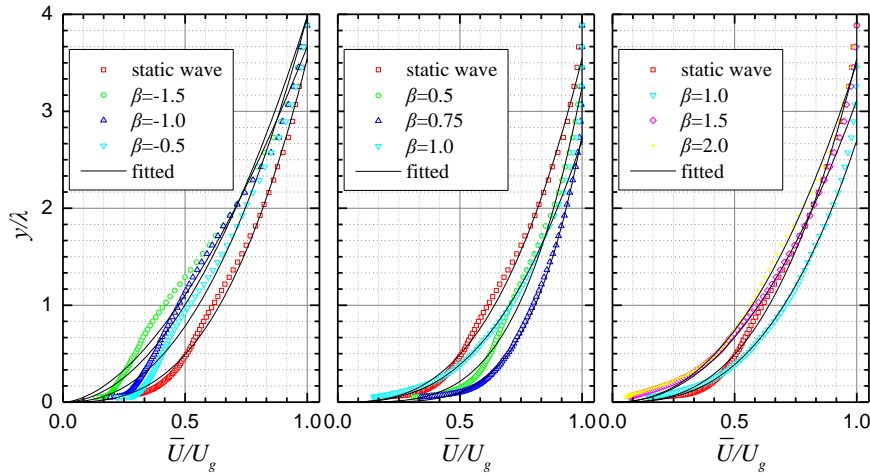


Fig. 9 Mean velocity profiles over waves fitted to power law expression

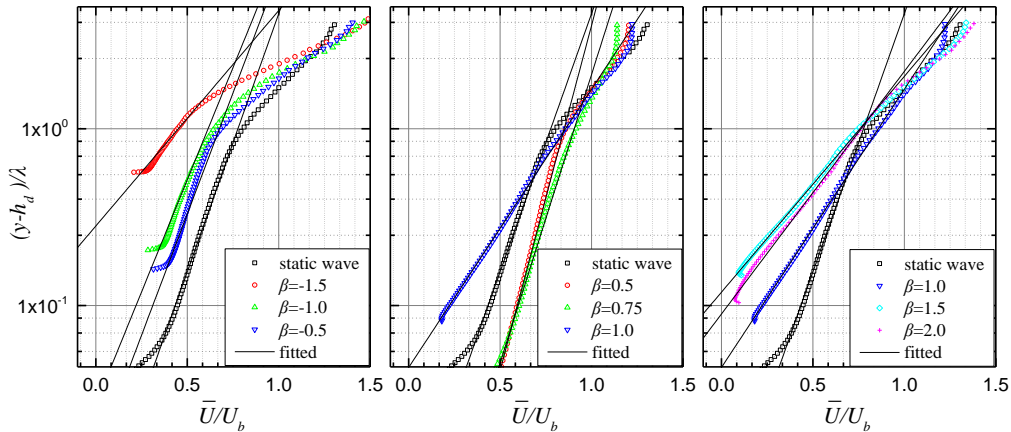


Fig. 10 Mean velocity profiles over waves fitted to log law expression

Table 1 Aerodynamic parameters of velocity profile over a wave

Wave Amp. $\xi$	Wave age $\beta$	Power law index $\alpha$	Grad. height $H_g/\lambda$	Grad. Velo. $U_g/U_b$	Fric. velo. $u_*/U_b$	Rou. length $h_0/\lambda$	Zero-disp. Height $h_d/\lambda$
0.025	-1.5	0.397	3.46	1.345	0.059	0.008	-0.049
	-1.0	0.362	3.26	1.306	0.047	0.002	-0.200
	-0.5	0.294	3.07	1.260	0.042	0.001	0.004
	static wave	0.238	2.04	1.101	0.055	0.001	0.015
	0.5	0.247	2.73	1.163	0.048	0.001	0.015
	0.75	0.215	2.29	1.126	0.050	0.001	0.014
	1.0	0.189	1.92	1.097	0.056	0.001	0.018
	1.5	0.264	2.73	1.193	0.077	0.011	-0.008
	2.0	0.358	2.90	1.218	0.094	0.028	-0.030
0.050	-1.5	0.578	>4.00	1.514	0.143	0.282	-0.517
	-1.0	0.504	3.67	1.470	0.069	0.028	-0.155
	-0.5	0.427	3.45	1.392	0.063	0.014	-0.110
	static wave	0.351	2.89	1.297	0.059	0.005	0.007
	0.5	0.255	2.58	1.195	0.045	0.001	0.038
	0.75	0.211	2.43	1.133	0.053	0.001	0.024
	1.0	0.357	2.72	1.211	0.110	0.044	-0.031
	1.5	0.451	3.26	1.326	0.142	0.119	-0.098
	2.0	0.446	3.67	1.379	0.127	0.090	-0.053
0.075	-1.5	0.636	>4.00	1.610	0.133	0.283	-0.560
	-1.0	0.645	>4.00	1.619	0.096	0.118	-0.348
	-0.5	0.578	3.67	1.536	0.091	0.089	-0.271
	static wave	0.413	3.46	1.355	0.085	0.028	-0.015
	0.5	0.256	3.26	1.219	0.056	0.002	0.034
	0.75	0.258	2.89	1.182	0.066	0.005	0.013
	1.0	0.439	3.26	1.298	0.137	0.094	-0.039
	1.5	0.582	3.46	1.402	0.167	0.186	-0.104
	2.0	0.549	3.67	1.421	0.194	0.221	-0.111

Table 1 summarizes the aerodynamic parameters associated with the velocity profile obtained by fitting the velocity profiles to the power law and log law expressions. Meanwhile, the change of gradient height and power law index, and the change of roughness length and friction velocity with wave age at different wave amplitudes, are illustrated in Figs. 11 and 12, respectively, in which the broken lines express the general tendency of variation. Fig. 11(a) shows that, for all three investigated wave amplitudes, the power law index exhibits a smallest value at around  $\beta = 0.75$ , rather than that of a static wave. When the wave moves downstream slower ( $0 < \beta < 1$ ) or a little faster than air ( $1 < \beta < 1.5$ ), the power law index is smaller than that of a static wave. When the wave moves downstream much faster than air ( $\beta > 1.5$ ) or moves against wind ( $\beta < 0$ ), the power law index is greater than that of a static wave and increases with increase in the absolute value of wave age. It is also shown in Fig. 11(a) that the power law index increases with increase in wave amplitude when the wave age is fixed. As for the results of the power law index, Fig. 11(b) shows that the lowest gradient height appears at around  $\beta = 0.75$  also at all three investigated wave amplitudes. The gradient height increases when the wave age becomes smaller or greater than 0.75, and increases with increase in wave amplitude. The variations of power law index and gradient height with wave age consistently show that, when the velocity difference between the wave and air is small, the wave plays a lesser aerodynamic role as surface roughness than a static wave in determining the structure of the boundary layer. However, the wave plays a greater aerodynamic role when the velocity difference becomes more obvious.

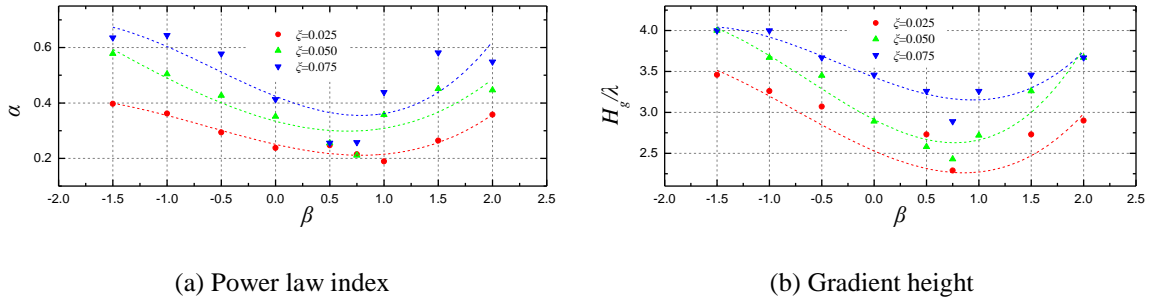


Fig. 11 Variations of power law index and gradient height with wave age

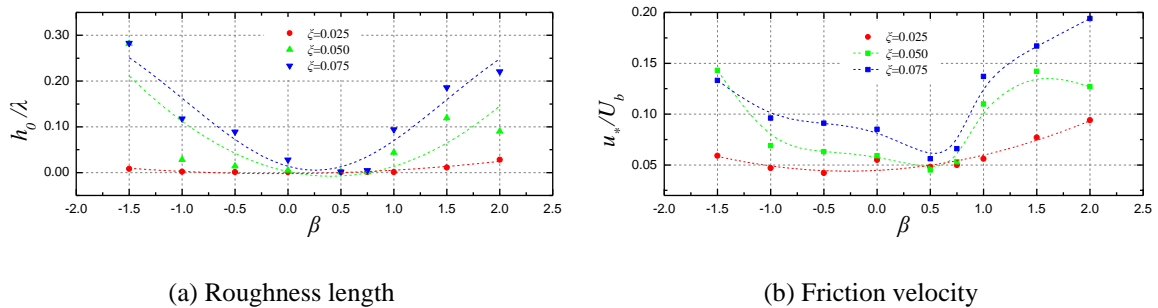


Fig. 12 Variations of roughness length and friction velocity with wave age

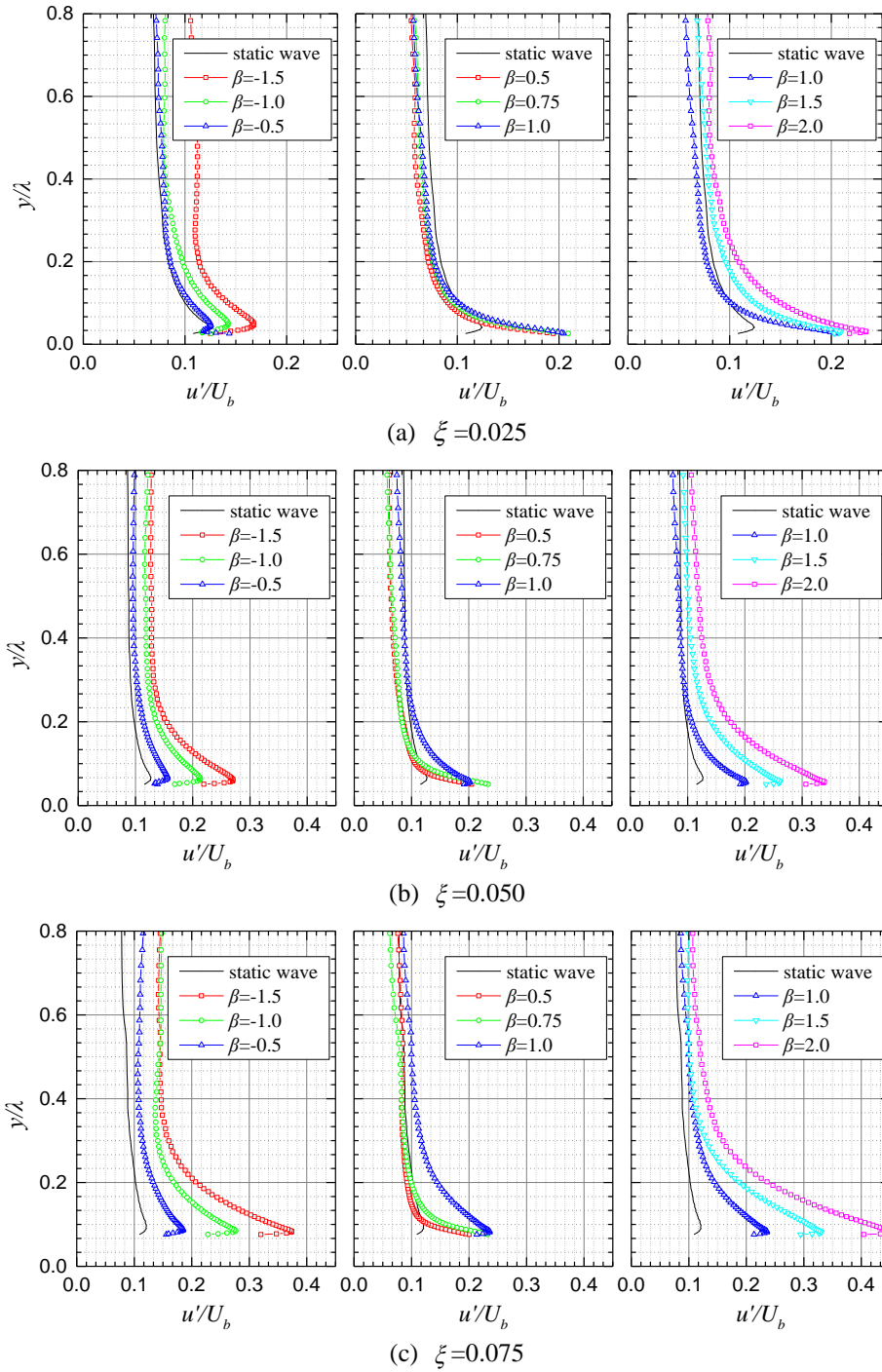


Fig. 13 Variation of fluctuating velocity profile with wave age at different wave amplitudes

This aerodynamic behavior of moving waves is also indicated in Figs. 12(a) and 12(b), in which the roughness length and friction velocity possess smallest values at around  $\beta = 0.5$ . Finally, it is necessary to emphasize that the large values of power law exponent or roughness length shown in Figs. 11 and 12 and in Table 1 are obtained at non-equilibrium wave conditions, which are assumed to be two-dimensional, periodic and non-evolving. These assumptions make the waves different from a real sea wave.

#### 4.3 Variation of fluctuating velocity profile with wave age and wave amplitude

Fig. 13 presents the variation of standard deviation of longitudinal velocity  $u'$  with wave age at different wave amplitudes. The standard deviations of longitudinal velocity for static waves with different wave amplitudes are shown together for comparison. It can be seen in Fig. 13 that, for all wave ages, the standard deviation of the fluctuating velocity at heights near the wave height is much greater than those of corresponding static waves. However, for heights above the wave height, they are smaller when wave age is  $\beta = 0.5, 0.75$  and  $1.0$ , or greater at other wave ages than those of static waves. In addition, it can be seen in Fig. 13 that there is a peak in the vertical profile of standard deviation, which appears at different heights. The peak is not visible at the profiles for  $\beta = 0.5$  and  $0.75$ , indicating that the peak height is lower than the wave height. For other wave ages ( $\beta > 1.5$  or  $\beta < 0$ ), the peak appears at heights very close to the peak heights for corresponding static waves. These results show that the flow becomes more turbulent when  $\beta > 1.5$  or  $\beta < 0$ , but become laminar to some degree when  $0 < \beta < 1.5$ , agreeing with the results of mean velocity profiles.

Fig. 14 illustrates the variations of profiles of turbulence intensity  $I_u$  with wave age, where the turbulence intensity is defined as  $I_u = u' / \bar{U}$ . The data obtained at wave age  $\xi = 0.05$  are shown as an example.

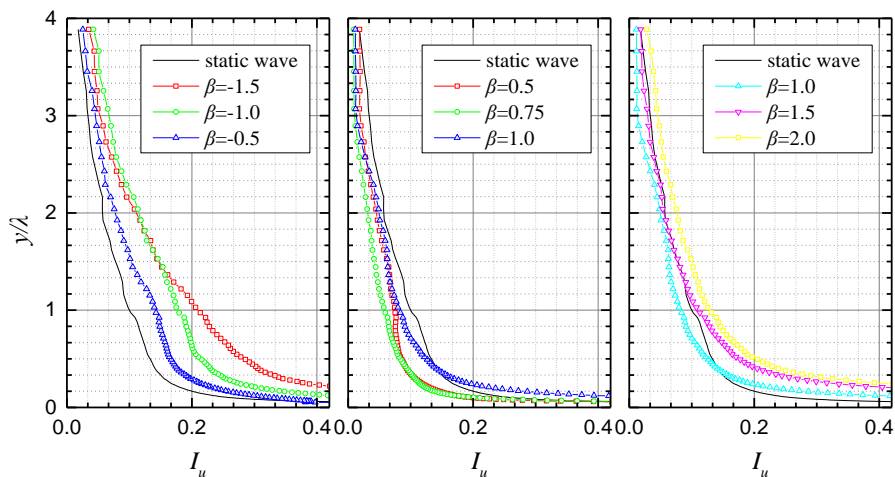


Fig. 14 Variation of turbulence intensity with wave age at  $\xi = 0.05$

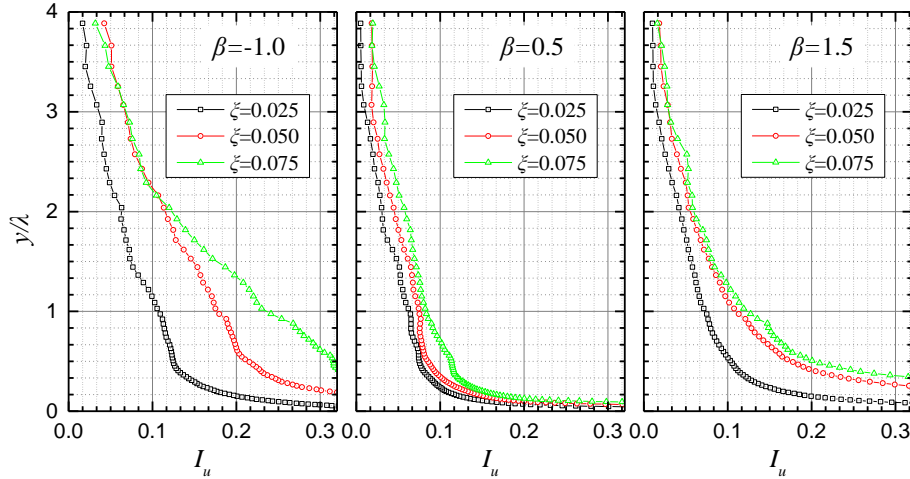


Fig. 15 Variation of turbulence intensity with wave amplitude

It is obvious that the turbulence intensity is greater than that of a corresponding static wave over the whole boundary layer height when the wave opposes wind ( $\beta < 0$ ) or moves much faster than wind ( $\beta > 1.5$ ). Turbulence intensity is lower when the wave follows wind ( $0 < \beta < 1.0$ ) at higher heights of the boundary layer. Fig. 15 presents the variation of turbulence intensity with wave amplitude by fixing the wave age. It is shown that the turbulence intensity increases with wave amplitude.

## 5. Conclusions

Large-eddy simulation of fully developed turbulent flow over an imposed undulating wave is presented for a bulk Reynolds number of 10000, in order to shed light on wind characteristics over sea waves for wind engineering applications. The variations of mean and fluctuating velocity profiles with wave age and wave amplitude are studied systematically. The change of gradient height and power law index, and change of roughness length and friction velocity with wave age are provided. When a wave moves downstream slower than air ( $0 < \beta < 1.0$ ) or a little faster than air ( $1.0 < \beta < 1.5$ ), it plays a lesser aerodynamic role as roughness and the flow becomes laminar to some degree. The gradient height, power law index, roughness length, friction velocity, and turbulence intensity are smaller than those of static waves. A moving wave plays a minimal aerodynamic role when wave age equals about 0.75. However, when a wave moves downstream much faster than air ( $\beta > 1.5$ ) or moves opposing air ( $\beta < 0$ ), it plays a more aerodynamic role. The gradient height, power law index, roughness length, friction velocity, and turbulence intensity increase. Furthermore, the wave becomes aerodynamically rougher when wave amplitude is increased.

Finally, it should be noted that the flow configuration considered in this study is simplified to

two-dimensional, periodic and non-evolving. A real sea wave cannot maintain values of wave age or wave amplitude as time advances. For a mature sea wave, an equilibrium value of wave age is about 1.2 (Alves *et al.*, 2003), and the wave age is most often either negative or greater than the equilibrium value. In addition, with increase in wave amplitude, the wave is likely to break. The simplification adopted in the present study may create errors if obtained results are directly applied to a real sea wave. As a result, more field measurements and analyses are necessary in order to achieve a better understanding of real wind over sea waves.

## Acknowledgements

This research was funded in part by the Natural Science Foundation of China (Project No: 51278366 and 51478358) and MOE Specialized Research Fund for the Doctoral Program of Higher Education of China (Project No: 20130072110007). The authors greatly appreciate constructive suggestions from Prof. Yukio Tamura of Tokyo Polytechnic University.

## References

- Architectural Institute of Japan (2004), AIJ-RLB-2004, Recommendations for Loads on Buildings, Maruzen, 651 (in Japanese)
- Alves, J.H.G.M., Banner, M.L. and Young, I.R. (2003), "Revisiting the Pierson-Moskowitz asymptotic limits for fully developed wind waves", *J. Phys. Oceanogr.*, **33**, 1301-1323.
- American Society of Civil Engineers (2010), *Minimum design loads for buildings and other structures*, ASCE 7-10, ASCE, Reston, Virginia.
- Buckles, J., Hanratty, T.J., Adrian, R.J. (1984), "Turbulent flow over large-amplitude wavy surfaces", *J. Fluid Mech.*, **140**, 27-44.
- Charnock, H. (1955), "Wind stress on a water surface", *Q. J. Roy. Meteor. Soc.*, **81**(350), 639-640.
- Chen, D. and Letchford, C.W. (2007), "A laboratory study of wind stress over simulated waves", *Proceedings of the 12th International Conference on Wind Engineering*, June 2-5, Cairns, Queensland, Australia.
- Drennan, W.M., Taylor, P.K. and Yelland, M.J. (2004), "Parameterizing the sea surface roughness", *J. Phys. Oceanogr.*, **35**(5), 835-848.
- Issa, R.I. (1986), "Solution of the implicit discretised fluid flow equations by operator-splitting", *J. Comput. Phys.*, **62**(1), 40-65.
- Johnson, H.K., Hfjstrup, J., Vested, H.J. and Larsen, S.E. (1998), "On the dependence of sea surface roughness on wind waves", *J. Phys. Oceanogr.*, **28**(9), 1702-1716.
- Jones, I.S.F. and Toba, Y. (2001), *Wind Stress over the Ocean*, Cambridge University Press.
- Lilly, D.K. (1992), "A proposed modification of the Germano subgrid-scale closure method", *J. Phys. Fluids*, **4**(3), 633-635.
- Niclasen, B.A., Simonsen, K. and Magnusson, A.K. (2010), "Wave forecasts and small-vessel safety: A review of operational warning parameters", *Marine Struct.*, **23**(1), 1-21.
- OpenFOAM. OpenFOAM user guide [M/OL], 2012.
- Powell, M.D., Vickery, P.J. and Reinhold, T.A. (2003), "Reduced drag coefficient for high wind speeds in tropical cyclones", *Nature*, **422**, 279-283.
- Shen, L., Zhang, X., Yue, D., Triantafyllou, M.S. (2003), "Turbulent flow over a flexible wall undergoing a streamwise travelling wave motion", *J. Fluid Mech.*, **484**, 197-221.
- Smith, S.D., Anderson, R.J., Oost, W.A., Kraan, C., Maat, N., De Cosmo, J., Katararos, K.B., Davidson, K.L., Bumke, K., Hasse, L. and Chadwick, H.M. (1992), "Sea surface wind stress and drag coefficients:

- the HEXOS results”, *Bound. – Lay. Meteorol.*, **60**(1), 109-142.
- Sullivan, P.P., Edson, J.B., Hristov, T. and McWilliams, J.C. (2008), “Large-eddy simulation and observations of atmospheric marine boundary layers above non-equilibrium surface waves”, *J. Atmos. Sci.*, **65**(4), 1225-1245.
- Sullivan, P.P. and McWilliams, J.C. (2002), “Turbulent flow over water waves in the presence of stratification”, *Phys. Fluids*, **14**, 1182-1195.
- Sullivan, P.P., McWilliams, J.C. and Moeng, C.H. (2000), “Simulation of turbulent flow over idealized water waves”, *J. Fluid Mech.*, **404**, 47-85.
- Toba, Y., Iida, N., Kawamura, H., Ebuchi, N. and Jones, I.S.F. (1990), “The wave dependence of sea-surface wind stress”, *J. Phys. Oceanogr.*, **20**, 705-721.
- Zachry, B.C., Letchford, C.W., Zuo, D. and Kennedy, A.B. (2013), “Laboratory measurements of the drag coefficient over a fixed shoaling hurricane wave train”, *Wind Struct.*, **16**(2), 193-211.
- Zachry, B.C., Schroeder, J.L., Kennedy, A.B., Westerink, J.J., Letchford, C.W. and Hope, M.E. (2013), “A case study of near shore drag coefficient behavior during Hurricane Ike (2008)”, *J. Appl. Meteor. Clim.*, **52**(9), 2139-2146.

JH